Influence of honeycomb structures on straight-through labyrinth seal aerodynamics

Check for updates

*Correspondence:
MO: oettinger@tfd.uni-hannover.de

Marcel Oettinger[1,*], Tim Kluge[1], Joerg Seume[1]

[1]Leibniz Universität Hannover, An der Universitaet 1, 30823 Garbsen, Germany

Abstract

Shroud cavities in aero engines are typically formed by a labyrinth seal between the rotating turbine shroud and the stationary casing wall. To mitigate rub-in and reduce weight, the casing often features honeycomb structures above the rotor seal fins. In this paper, the aerodynamic performance of such honeycomb structures is experimentally investigated using a rotating test rig featuring both smooth and honeycomb-tapered casing walls.

Measurements show that the discharge coefficient decreases for the honeycomb configuration while losses and subsequent windage heating of the flow increase. A variation in rotational speed reveals additional sensitivities to the local flow field in the swirl chamber. Numerical simulations are conducted and validated using the experiments. A good agreement between the prediction and measurements of the jet via the evolution of pressure across the sealing fins is identified. In contrast, the prediction of losses and integral parameters reveals larger deficits.

Empirical correlations from available literature satisfactorily predict the leakage mass flow rate if rotation is low and if the casing is smooth. High rotation and the presence of honeycombs, however, prove challenging and reveal the potential for further improvements. We propose a simple a-posteriori correction that can capture the effect of honeycomb structures on seal discharge by accounting for changes in momentum and flow area.

Introduction

Modern aero-engine low-pressure turbines, particularly high-speed turbines in decoupled architectures such as geared turbo fans, often feature a shrouded design to improve structural integrity. In terms of aerodynamics, shrouds eliminate the tip gap vortex. However, a cavity is formed between the rotating shroud and the stationary casing, giving rise to new and complex flow features inside the cavity.

Increasing the efficiency of shroud seals is thus an increasingly important task. Shroud cavities are usually designed as stepped labyrinth seals, where a rub-in coating or more complex, three-dimensional structures form the casing contour. The latter are particularly beneficial in terms of weight reduction and mitigating rub-in risk.

Steady-state evaluation of labyrinth seals can be characterized by two factors: The leakage mass flow or discharge and its accompanying dissipation of kinetic energy. The more leakage-flow momentum is dissipated, the lower the mass-flow rate but the higher the subsequent flow heating - which is critical for the structural integrity if the local component temperature is increased beyond tolerance. Understanding and predicting aerodynamic performance is thus of critical importance for the design of advanced seal configurations.

One of the earliest experimental works concerning the influence of honeycomb lands was conducted by Stocker et al. (1977) who designed a rotating rig for straight-through labyrinth seals. Stocker et al. found seal leakage to decrease for honeycomb lands compared to a smooth wall, unless the honeycomb cells were very wide compared to the clearance. Tipton et al. (1986) obtained similar results.

For stepped labyrinth seals, several authors observed an inverse trend with honeycomb lands increasing the leakage mass-flow rate (Schramm et al., 2002; Yan et al., 2010). Other authors, however, found leakage to decrease even in stepped labyrinth seals (McGreehan and Ko, 1989). Schramm et al. (2002) argue that the leakage decrease in straight-through seals compared to stepped seals results from the flow more directly interacting with the honeycomb, with the honeycomb acting as a rough surface dissipating the kinetic energy of the leakage flow. This dissipation counter-acts the observed increase in the effective clearance as flow enters the honeycomb. The performance of labyrinth seals with honeycomb lands thus greatly depends on the topology of the seal. Other geometric parameters to consider are those of the honeycomb geometry itself, particularly the ratio of fin width to honeycomb diameter and clearance (Zimmermann and Wolff, 1998; Schramm et al., 2002).

Experimental studies (such as Waschka et al., 1991; Denecke et al., 2004; Paolillo et al., 2007) using rotating rigs as well as numerical studies (Yan et al., 2009; Li et al., 2010; Nayak and Dutta, 2015) stress the importance of rotation on labyrinth seal performance. The discharge coefficient decreases for higher rotational speed while the flow heating or windage loss increases. Similarly, pre-swirl can have a drastic effect on windage heating by increasing or deceasing the wall shear stresses, depending on the swirl angle being positive or negative (McGreehan and Ko, 1989; Yan et al., 2010).

In the present work, the influence of honeycomb structures on aerodynamic performance is investigated in a rotating straight-through labyrinth seal test rig. Two configurations are studied: a smooth and a honeycomb-tapered casing. The comparison of both configuration aims at answering the following questions:

- What is the influence of honeycomb structures on flow aerodynamics in turbine shroud straight-through labyrinth seals?
- How does the labyrinth seal performance behave at different operating points?
- How well can local and integral flow parameters be predicted by numerical RANS simulations and reduced-order correlations?

Methodology

To compare the leakage mass flow rate across different configurations at different operating conditions, we use the discharge coefficient

$$C_D = \frac{A_m}{A_{gap}} = \frac{\dot{m}}{\dot{m}_{id}} \tag{1}$$

relating the minimum flow area A_m at the seal to the geometric flow area A_{gap} (see Figure 1). In incompressible flow, this is equivalent to relating the actual mass flow to that of an ideal nozzle at the same operating conditions

$$\dot{m}_{id} = \frac{A_{gap} p_{t,in}}{\sqrt{T_{t,in}}} \left(\frac{p_{out}}{p_{t,in}}\right)^{1/\kappa} \sqrt{\frac{2\kappa}{R(\kappa - 1)} \left(1 - \left(\frac{p_{out}}{p_{t,in}}\right)^{((\kappa-1)/\kappa)}\right)} \tag{2}$$
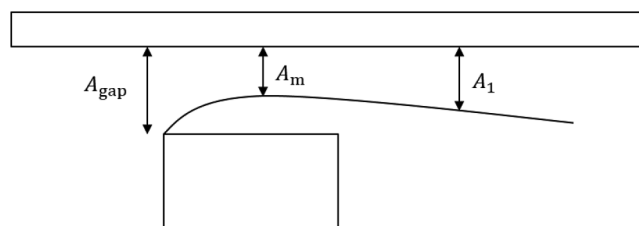

Figure 1. Schematic depiction of discharge at the shroud seal.

The flow coefficient α relates the jet area to the geometric area,

$$\alpha = \frac{A_1}{A_{\text{gap}}} \tag{3}$$

Flow and discharge coefficient are related via the contraction coefficient C_C where

$$C_D = \alpha \frac{A_m}{A_1} = \alpha C_C \tag{4}$$

In the literature several correlations to estimate the mass flow rate across a labyrinth seal can be found. For the present work we utilize the correlation by Egli (1935)

$$\dot{m}_{\text{Egli}} = \frac{\varphi \gamma \alpha A_{\text{gap}} p_{\text{t,in}}}{\sqrt{R T_{\text{t,in}}}} \tag{5}$$

where φ is a term accounting for the expansion work done on the fluid between the n throttlings of the labyrinth seal which was first formulated by Martin (1919)

$$\varphi = \sqrt{\frac{1 - \left(p_{\text{out}}/p_{\text{t,in}}\right)^2}{N + \ln\left(p_{\text{t,in}}/p_{\text{out}}\right)}} \tag{6}$$

For the carry-over coefficient γ and the flow coefficient α, values according to the geometric labyrinth seal parameters were selected as a function of rotational speed and the measurements of Egli (1935). Windage heating is assessed by calculating the total temperature increase across the seal rig via

$$\dot{Q}_W = \dot{m}c_p(T_{\text{t,out}} - T_{\text{t,in}}) \tag{7}$$

Assuming an adiabatic system, windage heating can be related to flow losses using the estimation of entropy production

$$\dot{s} = k_{\text{eff}}\left(\frac{\partial T}{\partial x_j}\right)^2 + \mu_{\text{eff}}\left(\frac{\partial U_i}{\partial x_j} + \frac{\partial U_j}{\partial x_i}\right)\frac{\partial U_i}{\partial x_j} = c_p\left(\frac{\mu}{\text{Pr}} + \frac{\mu_T}{\text{Pr}_T}\right)\left(\frac{\partial T}{\partial x_j}\right)^2 + (\mu + \mu_T)\left(\frac{\partial U_i}{\partial x_j} + \frac{\partial U_j}{\partial x_i}\right)\frac{\partial U_i}{\partial x_j} \tag{8}$$

as derived by Moore and Moore (1983), where the first term on the right-hand side describes losses due to internal heat transfer and the second term denotes viscous dissipation. In both, turbulence is accounted for by including the eddy viscosity μ_T and the turbulent Prandtl number $\text{Pr}_T = 0.9$. In the experiment, the influence of rotation is assessed while maintaining a constant corrected rotational speed

$$n_{\text{red}} = n\sqrt{\frac{T_{\text{t,in}}}{T_{\text{t,ref}}}} \tag{9}$$

across different configurations and operating conditions. The corrected speed is related to the reference speed of the aerodynamic design point (ADP) via

$$n_{\text{rel}} = \frac{n_{\text{red}}}{n_{\text{red,ref}}} = \frac{n_{\text{red}}}{n_{\text{red,ADP}}} \tag{10}$$

Test case

Experimental setup

The Institute of Turbomachinery and Fluid Dynamics operates a rotating labyrinth seal rig first described in Kluge et al. (2019). This rig permits investigating different turbine shroud cavity geometries experimentally at rotational speeds representative of low-pressure turbines. Kluge et al. (2020), e.g., previously investigated unsteady flow phenomena in the shroud cavity.

The test rig as depicted in Figure 2 employs a rotating disk mounted on a shaft driven by an electric motor. Air enters the rig through a volute inducing pre-swirl with a flow angle derived from the turbine rig described in Henke et al. (2016). The cavity is formed by the seal fin geometry carried by the rotating disk and the outer casing. For the present investigation, two different casing rings were manufactured. Both rings differ only in the area marked *Variable geometry* in Figure 3 with one ring featuring a smooth rub coating similar to that of a turbine and the other featuring a honeycomb structure.

For this investigation of the honeycomb influence on seal flow characteristics, only the cavity geometry deviates from the general rig geometry first documented in Kluge et al. (2019). While the rotor is identical, the casing geometry has been modified. It comprises a constant-annulus section immediately above the rotating disk and two discontinuous changes in diameter upstream and downstream of this section (forward and backward facing steps). The configuration is shown in detail in Figure 3a. The cavity geometry can be subdivided into three sections: The cavity inlet region (K1), the swirl chamber (K2) and the cavity outlet region (K3).

At the rig inlet and outlet planes total pressure and temperature are measured using rake probes while wall taps at the hub and tip casing deliver the static pressure. The mid-span position of each rake is executed as a three-hole probe which yields the respective inlet and outlet flow angles. Additional wall taps line the casing wall at the cavity. Several axial positions—see Figure 3a—are used to obtain the axial pressure distribution, yielding not only the pressure upstream and downstream of the cavity, but also inside the swirl chamber. At K1.1, K2.2 and K3.3 six equidistant circumferential positions exist. For the configuration including the honeycomb structure, additional wall taps were introduced to obtain a more refined pressure distribution. These refinement positions comprise three equidistant circumferential positions. Both K1 and K3 also feature thermocouples near the casing, which are used to measure the change in static temperature across the swirl chamber. Uncertainties within a 95% interval of confidence were obtained for all measurements and derived variables in the experiment.

In order to isolate the honeycomb influence, a constant pressure ratio and corrected rotational speed is maintained for both configurations. Flow and test parameters are listed in Figure 3b. Rotational speeds ranging from $n_{rel} = 1\%$ to 100% and pressure ratios ranging from $\Pi_{rel} = 80\%$ to 100% of those at the nominal operating point were experimentally investigated.
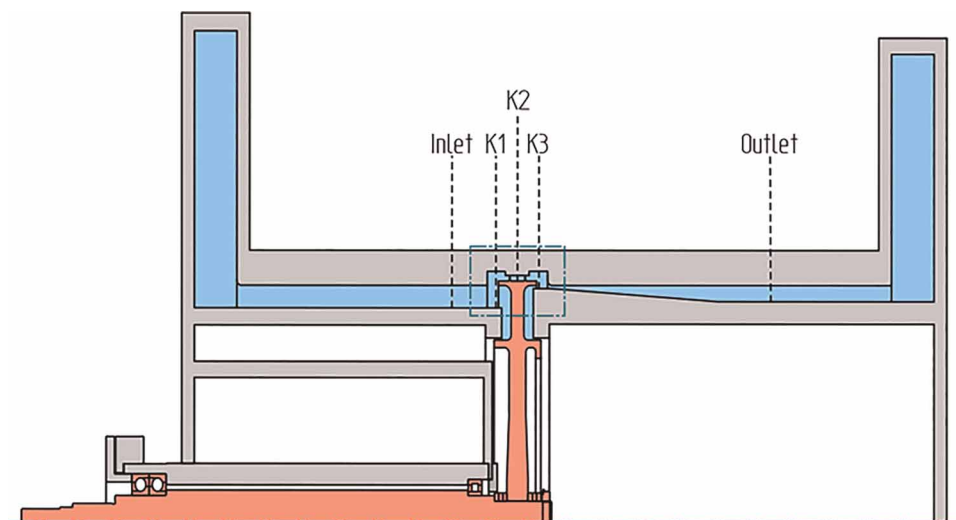

Figure 2. Schematic depiction of the rotating labyrinth seal test rig (Rotated by 90°).
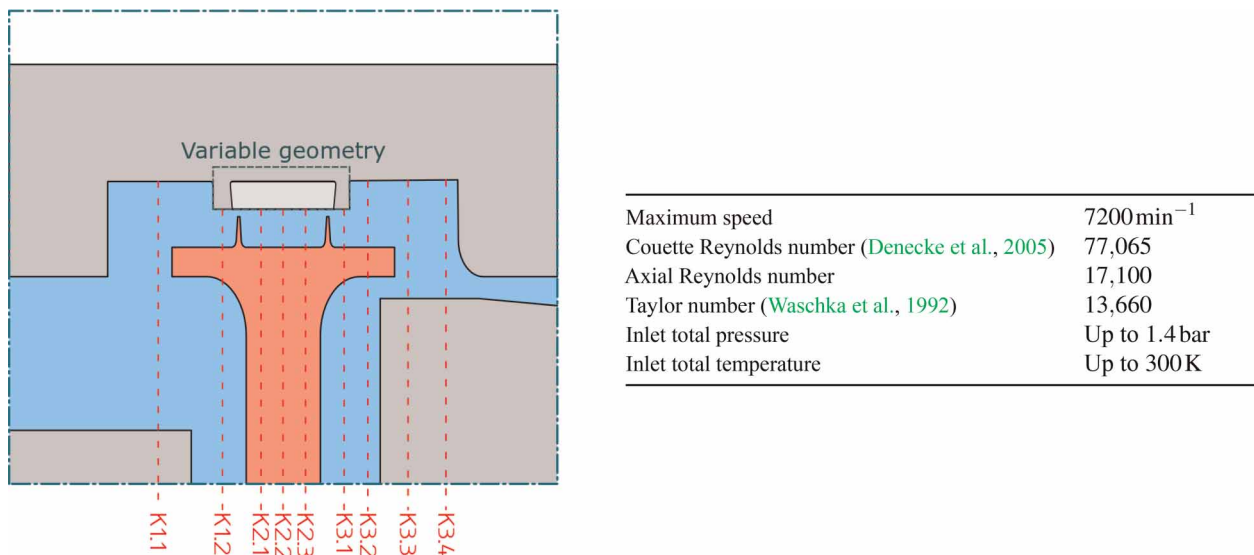
Maximum speed	$7200\,\mathrm{min}^{-1}$
Couette Reynolds number (Denecke et al., 2005)	77,065
Axial Reynolds number	17,100
Taylor number (Waschka et al., 1992)	13,660
Inlet total pressure	Up to 1.4 bar
Inlet total temperature	Up to 300 K

Figure 3. Measurement positions inside cavity (left) and operating conditions of the test rig (right).

Numerical model

Steady-state simulations have been conducted using the TRACE solver (Franke et al., 2005), which is developed by the German Aerospace Center and MTU Aero Engines AG. The computational grid is shown (distorted for better visibility) in Figure 4. A periodic segment size of $1.5°$ has been chosen for the numerical simulations, as for the steady state simulation no periodic phenomena exceeding a honeycomb pitch $(0.75°)$ are expected. The segment size thus corresponds to four honeycomb cells in circumferential direction (Figure 4b). The main domain blocking consists of two O-grids wrapping around the hub and casing walls. A dimensionless wall distance of the first grid cell equalling $y^+ < 1$ is adhered to at every point. A singular honeycomb is meshed using an O-grid and then duplicated to match the manufactured structure. Unlike the main flow domain, the honeycomb walls are not resolved by the grid; instead wall functions are used. The main flow domain comprises 1,770,890 cells while the honeycomb structure totals 4,478,600 cells across all combs.

In circumferential direction, a periodic boundary condition is prescribed. The rotor is specified as a moving wall with the absolute speed of the experiment. At the inlet, radial profiles as obtained by experimental data (rake probes) are prescribed while the experimental back-pressure at the casing acts as the outlet boundary condition. The influence of centrifugal forces on the rotor diameter is accounted for by adjusting the radial gap size individually for every investigated speed on the basis of results obtained from structural simulations. For the honeycomb configuration, a fluid-fluid interface connects the main flow domain to the honeycomb domain. This interface allows for the direct transfer of information to the neighbouring domain via interpolation. In case an interface node in the main domain has no partner on the honeycomb side, a local no-slip wall treatment is prescribed instead.

A second-order accurate Fromm scheme (Darwish, 1993) with the van Albada limiter (van Albada et al., 1982) is employed for spatial discretization while a second-order central difference scheme is used to solve the
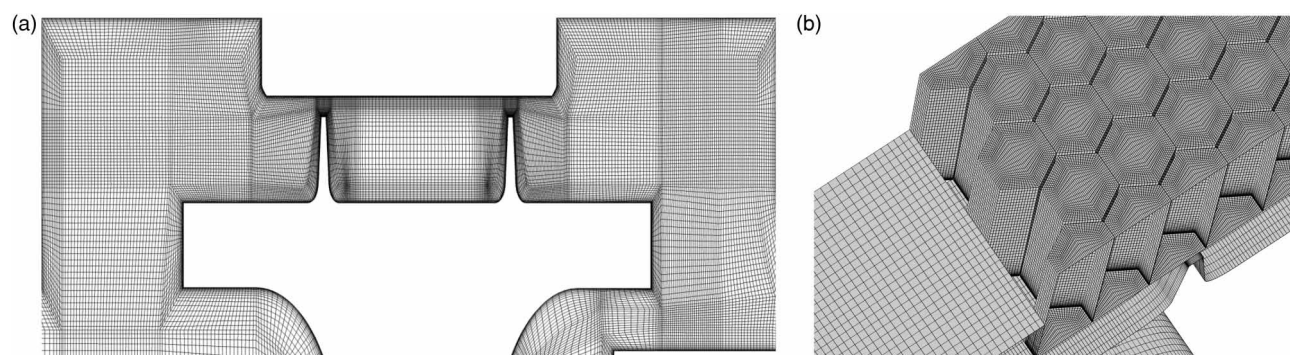

Figure 4. Computational grid. (a) Main domain (only every second node shown). (b) Honeycomb grid.

viscous fluxes. The Wilcox 1988 $k - \omega$-model (Wilcox, 1998) is used to model turbulence, using the correction by Kato and Launder (1993) to account for turbulent kinetic energy production near the stagnation points.

The mesh described has been derived by means of a grid independence study in accordance with the guidelines of the ASME V&V Committee (2009). The influence of spatial discretization is assessed by way of the grid convergence index according to Roache (1994), calculated for the discharge coefficient:

$$\text{GCI} = \frac{F_S e_a}{\mathfrak{R}^\rho - 1} \tag{11}$$

The reference grid has been both coarsened and refined by a factor of $\mathfrak{R}_{32} = \mathfrak{R}_{12} = 0.5$, i.e. $N_1 < N_2 < N_3$. The distance of the first cell to the wall was kept constant when altering the mesh resolution. As per the ASME V&V Committee (2009), a factor of safety $F_S = 1.25$ has been used. The relative error e_a of the discharge coefficient decreases with grid refinement (Table 1), approximating a logarithmic behaviour. The error relative to the estimated Richardson result (EERE) of the reference grid is $\text{EERE}_{32} = 2.6\%$. Indeed, the discharge coefficient only changes by 4.9×10^{-3} when comparing the reference and fine grids. We can thus preclude a significant grid influence on the numerical results obtained on the reference grid.

All simulations featuring a smooth casing converged to an average residual of $L_1 < 3 \times 10^{-7}$ and a maximum residual of $L_{\max} < 1 \times 10^{-5}$. Due to the more complex flow interaction, residuals of the honeycomb configuration are higher, equalling $L_1 < 5 \times 10^{-7}$ and $L_{\max} < 5 \times 10^{-4}$, respectively.

Results and discussion

Effect of honeycomb structures on local flow field

We initially consider the influence of honeycomb structures on the local flow field at the nominal operating point (ADP). The axial pressure distribution through the test rig is depicted in Figure 5 using a pressure

Table 1. Grid Convergence Index of the discharge coefficient.

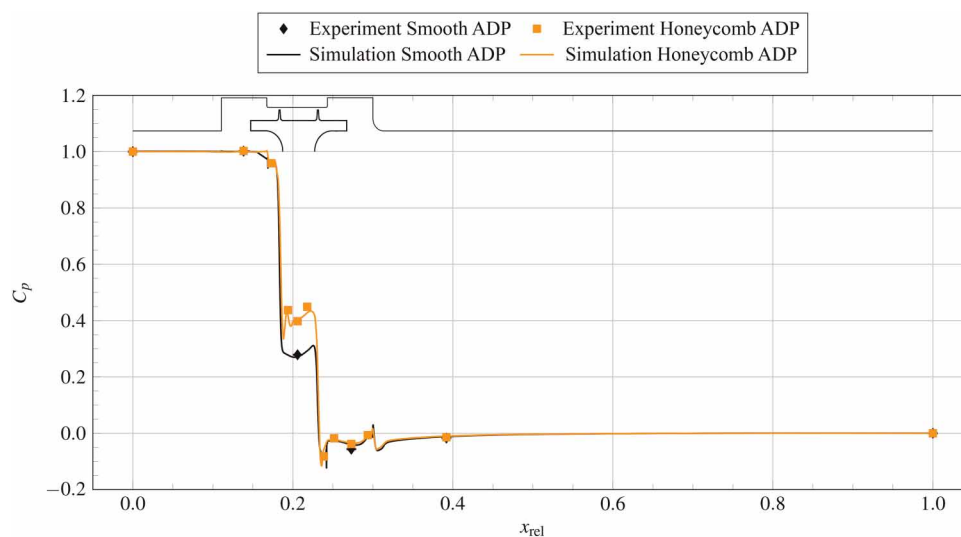| $C_{D,1}$	$C_{D,2}$	$C_{D,3}$	e_a^{21}	e_a^{32}	ϱ	EERE_{21}	EERE_{32}	GCI_{21}	GCI_{32}
0.5994	0.5923	0.5874	0.01180	0.00823	0.55	0.0395	0.0264	−0.0475	−0.0322

Figure 5. Comparison of axial pressure distribution for $n_{\text{rel}} = 100\%$ and $\Pi_{\text{rel}} = 100\%$. Error bars indicating 95% confidence interval are smaller than symbol size.

coefficient

$$C_p = \frac{p - p_{out}}{p_{t,in} - p_{out}}$$

(12)

for both experiment and numerical simulation. As mentioned above, the measurement resolution has been refined for the honeycomb configuration while the smooth configuration features fewer measurement positions in axial direction. Comparing experiment and numerical simulation, we are able to demonstrate a high agreement in all measurement planes.

In the flow regions upstream of the first fin and downstream of the second fin the normalised pressure is nearly identical. As is apparent in Figure 5, the key difference is thus the pressure drop across both throttlings, i.e. how the total pressure drop is split across the geometry. For the configuration with a honeycomb structure at the casing, the drop across both sealings is almost equal, while the smooth configuration shows a larger drop over the first seal fin and a smaller drop across the second one. Within the swirl chamber, i.e. between both fins, a deviation in the trend can also be identified. While the honeycomb configuration shows the pressure rising and falling in several sections, the smooth case shows an initially falling pressure followed by a stronger increase immediately upstream of the second fin.

The circumferentially mass-averaged flow field of both the main flow domain and the honeycomb domain inside the swirl chamber is depicted in Figure 6. Upstream of the first fin, the flow field is accelerated due to the forward-facing step, as is evident in the initial pressure drop at $x_{rel} = 0.18$ in Figure 5. A small separation bubble is present at the front section of the inner casing wall. This separation region is smaller for the smooth configuration, as the manufacturing process results in a small chamfer at this location. This chamfer is not present in the honeycomb structure. The flow contraction at the first fin is apparent, resulting in a smaller effective area compared to the actual geometry. At the honeycomb casing, a more complex interaction is visible: Due to the honeycomb structure, the effective flow area is enlarged. In the smooth case, the jet remains attached to the casing wall across the entire swirl chamber. The flow is strongly accelerated across the first throttling, followed by a deceleration upstream of the second fin. The aerodynamic cross-section of the jet increases throughout the swirl chamber. Here, the jet widens considerably more than in the former case. The vortex forming inside the swirl chamber is impacted by the increasing jet area. At the second fin, a similar area increase can be observed for the honeycomb case.

Based on the geometry of the honeycomb structure investigated, two extreme positions are identified at $\theta = 0.375°$ and $\theta = 0.75°$. Discrete circumferential slices are shown in Figure 7. At $\theta = 0.75°$, both fins are opposite of a honeycomb opening and the effective area at both fins increases. The honeycomb wall immediately downstream of the first throttling, however, radially deflects the jet towards the rotor, "cutting" into the swirl-chamber vortex before again turning towards the casing. This marks a subsequent decrease in effective flow area downstream of the fins. After four combs, the radial flow gradient is considerably diminished and the vortices inside the honeycombs almost act as a smooth boundary. At $\theta = 0.375°$, both fin positions overlap with a honeycomb wall causing a constriction in flow area at the throttling. Since the honeycomb geometry is
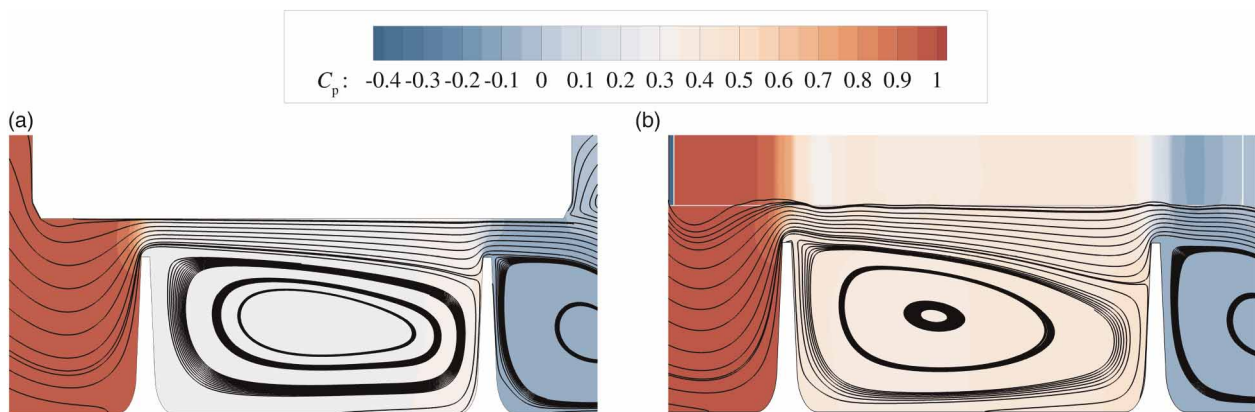

Figure 6. Comparison of circumferentially averaged flow field in the swirl chamber for $n_{rel} = 100\%$ and $\Pi_{rel} = 100\%$. (a) Smooth casing. (b) Honeycomb casing.
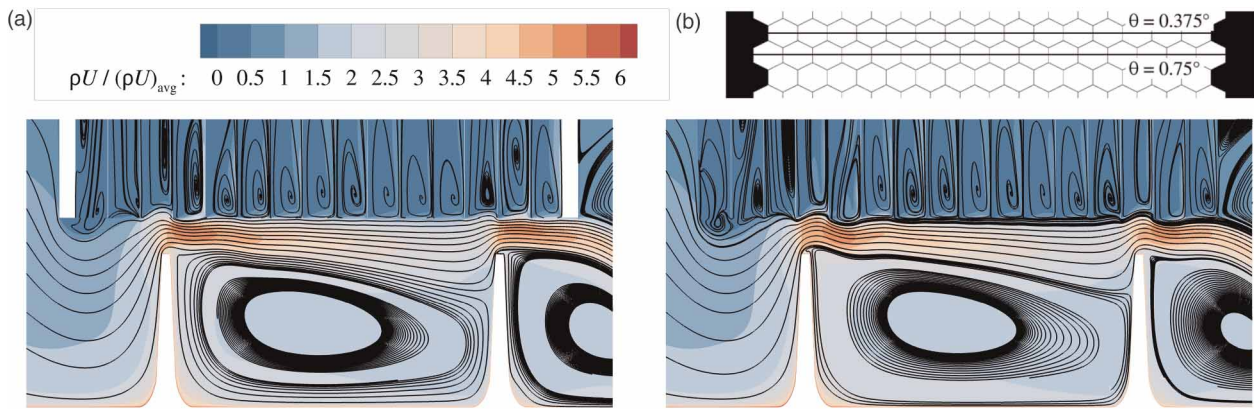
Figure 7. Flow field at discrete circumferential positions of the honeycomb configuration for $n_{\mathrm{rel}} = 100\%$ and $\Pi_{\mathrm{rel}} = 100\%$. (a) $\theta = 0.375°$. (b) $\theta = 0.750°$.

hexagonal, whenever a honeycomb wall is located above a fin, other circumferential positions feature the widest honeycomb area. The mean area remains constant in circumferential direction. The axial spacing only has a small influence, numerical studies showed no sensitivity to altering the axial honeycomb location. Comparing the detailed flow fields of Figure 7 to the resulting circumferential average in Figure 6, we can infer a net increase in flow area immediately at the fins and a net decrease in flow area downstream of the fins.

Influence of rotation

Additional influences on the local flow field are considered by evaluating the effect of rotation. The nominal operating point (ADP) features the maximum rotational speed investigated. In Figure 8 the axial pressure distributions at differing rotational speeds and at a constant pressure ratio of $\Pi_{\mathrm{rel}} = 90\%$ are depicted as well as their corresponding circumferentially mass-averaged flow fields. Entropy production is normalized to the mean production at the ADP for the smooth configuration to establish a common reference. The axial pressure distribution in
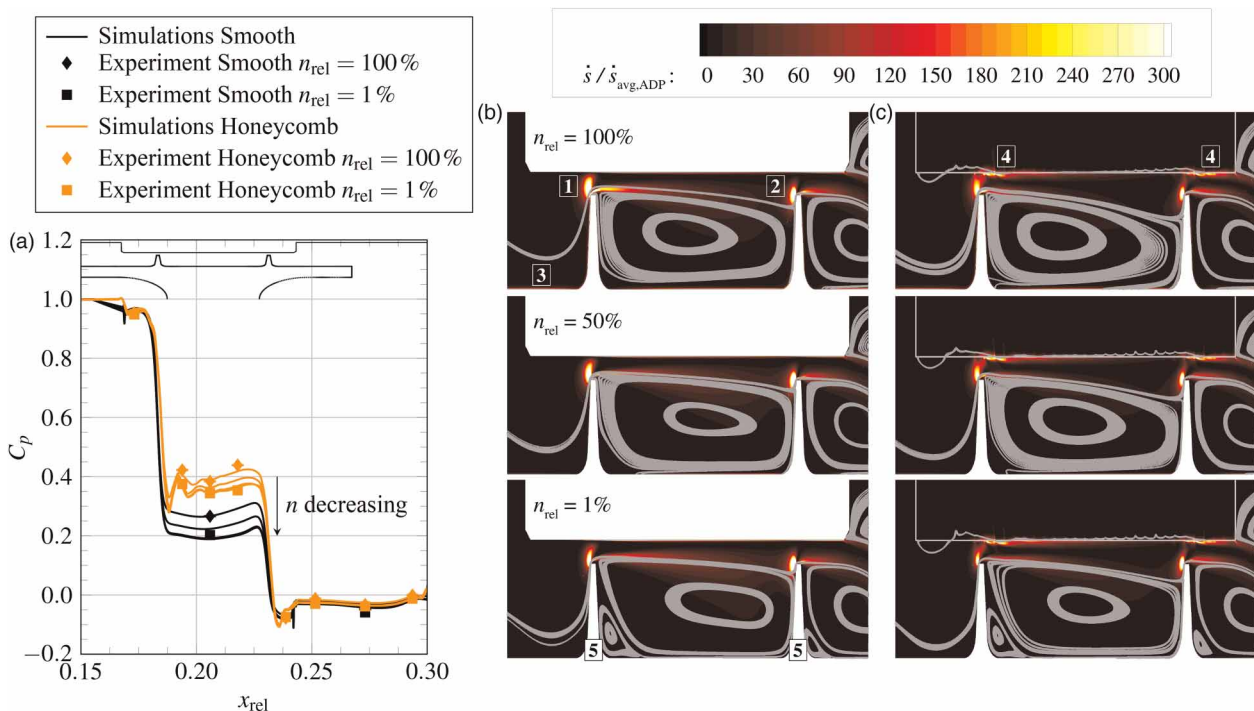

Figure 8. Influence of rotational speed on pressure distribution and entropy production for $\Pi_{\mathrm{rel}} = 90\%$. Error bars in (a) indicating 95% confidence interval are smaller than symbol size. (a) Axial distribution. (b) Smooth casing. (c) Honeycomb casing.

Figure 8a focuses on the section inside the swirl chamber, as no variation exists in the upstream and downstream sections. Rotational speeds considered are $n_{rel} = 100\%$, $n_{rel} = 50\%$, $n_{rel} = 10\%$ and $n_{rel} = 1\%$. For clarity, only the experimental data of the highest and lowest speeds are included in the plot.

Both experiment and numerical simulation agree well with regard to the axial pressure distribution. The pressure drop again occurs almost equally across both throttlings for the honeycomb case while it is higher at the first fin for the smooth case. The swirl chamber pressure is thus higher for the honeycomb configuration. For both cases, the relative (to the second fin) pressure drop across the first fin increases with a decrease in rotational speed. Additionally, a change in trend inside the swirl chamber can be observed, with the distributions becoming flatter. This effect is more pronounced in the honeycomb configuration, which can be captured by the numerical simulation as well.

Considering the circumferentially averaged flow fields in Figures 8b and c, several characteristic effects can be observed:

- The high velocity gradient immediately upstream of the first [1] and second [2] fins induced by the sudden acceleration across the throttling causes a significant rise in entropy production, i.e., loss. On top of the fins, local flow separation occurs. This separation likewise causes viscous dissipation inside the shear layer to the main flow. For the smooth configuration, these are the main source of loss, while this effect is weaker for the honeycomb configuration. Considering the streamlines, an increase in rotational speed results in more flow being entrained by the rotor and thus in an increase in the size of this separation bubble. While entropy production upstream of the first fin shows a dependency on rotational speed, it remains largely the same at the second fin regardless of speed.
- At the rotating walls [3] friction induces losses. This contribution appears to be identical for both configurations as only a function of speed and reaches almost zero for $n_{rel} = 1\%$.
- Friction at the honeycomb-tapered wall [4] is a considerable contribution to the total losses and marks the primary driver for increased losses in the honeycomb configuration. This effect is strongest immediately downstream of the fins and diminishes along a given streamline, correlating to the regions of strong main-flow-honeycomb interaction observed in Figure 7. No significant dependency on rotational speed appears to exist.
- The widening of the jet between both fins shows a strong sensitivity to the rotational speed, particularly for the honeycomb configuration. With an area increase of the jet, the cross-section of the swirl-chamber vortex decreases in turn.
- For zero and very low rotational speeds (e.g. $n_{rel} = 1\%$), additional vortices form at the rotor-shroud wall immediately downstream of the fins [5]. These structures are suppressed by rotation which causes the primary vortex to increase in size.

Integral parameters

The measured discharge coefficients for various rotational speeds and pressure ratios are depicted in Figure 9. Also included are the numerical results at $n_{rel} = 100\%$. As is to be expected, the discharge coefficient decreases for an increase in rotational speed which may be attributed to the contraction of the throttling area at the fins and a reduction of the carry-over of kinetic energy from the first to the second fin due to increased leakage jet dispersion and higher flow losses at the rotating walls. The two lowest rotational speeds ($n_{rel} = 1\%$ and $n_{rel} = 10\%$) almost overlap across the maps. While the numerical simulations are able to predict the pressure distribution across the seal satisfactorily, comparing the discharge coefficient shows significant discrepancies. Kluge et al. (2019) have shown that the discharge coefficient is sensitive to parallel changes in seal clearance, while the pressure distribution is mainly affected by asymmetric differences in the clearance. Thus, a difference in experimental and simulated radial clearance - even one within the measurement uncertainty of the clearance - may account for the offset.

The discharge coefficient of the investigated honeycomb structure is lower than that of the smooth configuration for all speed lines investigated. While the total pressure drop remains the same, the mass flow rate through the labyrinth seal decreases, in line with the observed higher losses. Considering windage heating (Figure 10), higher dissipation of kinetic energy is apparent. At the nominal operating point, the temperature difference between the boundaries of the control domain increases by 37% in the experiment. As the mass flow rate decreases by 8%, windage heating as the product of both contributions increases. A similar trend exists for all operating points along the nominal speed line. For operating points at lower speeds, differences are considerably smaller. Since the jet inside the swirl chamber was shown to increase in size if the rotational speed increases, friction between it and the swirl-chamber vortex are likely the main driver for loss, in addition to the local
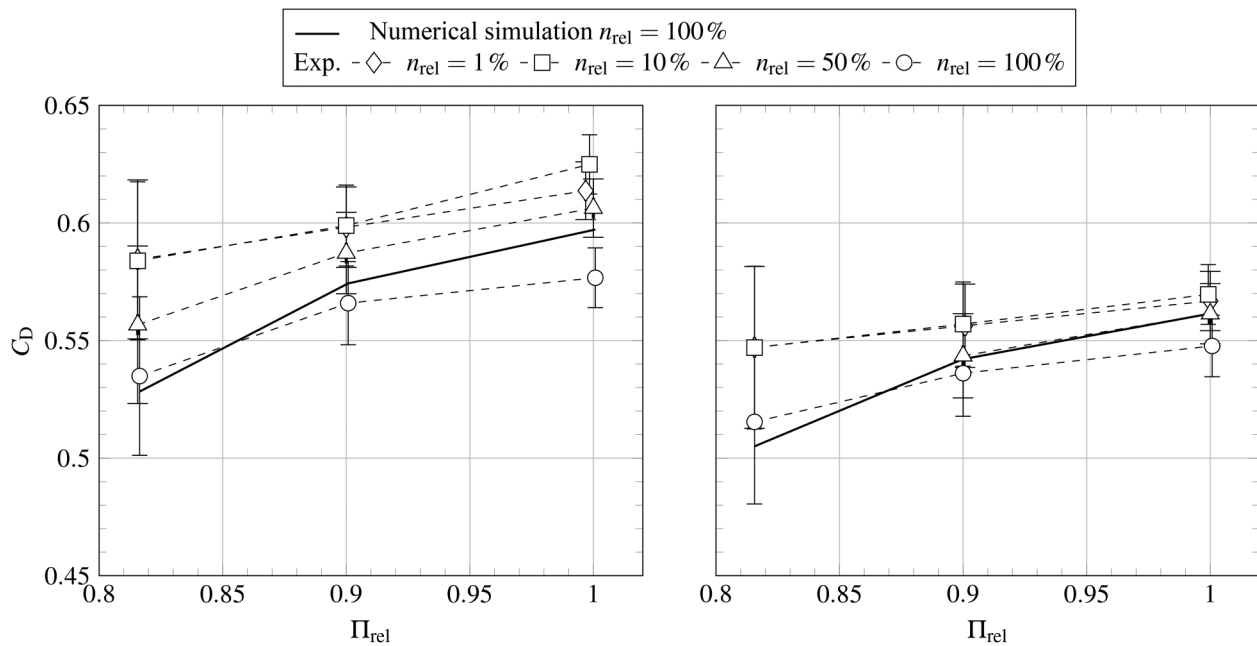
Figure 9. Discharge coefficient for smooth (left) and honeycomb (right) configurations. Error bars indicate 95% confidence interval.

dissipation at the honeycombs. The sensitivity to honeycomb structures is, however, much lower in the numerical simulation, where the calculated windage heating is almost the same for both configurations.

Even though the numerical simulations were demonstrated to capture the pressure drop across the labyrinth seal well, the prediction of integral parameters shows considerable deficits. Only for the lowest pressure ratios of the smooth and honeycomb configurations a good agreement can be found. At the higher pressure ratios, the discharge coefficient is over-predicted by 3.6% for the smooth and 2.6% for the honeycomb configuration. Previous investigations (Kluge et al., 2019) have demonstrated a considerable impact of the gap size on the mass flow rate while RANS-models are known to mis-predict the dragging effect of the rotor (Wein et al., 2020) which becomes more pronounced for high rotational speeds.
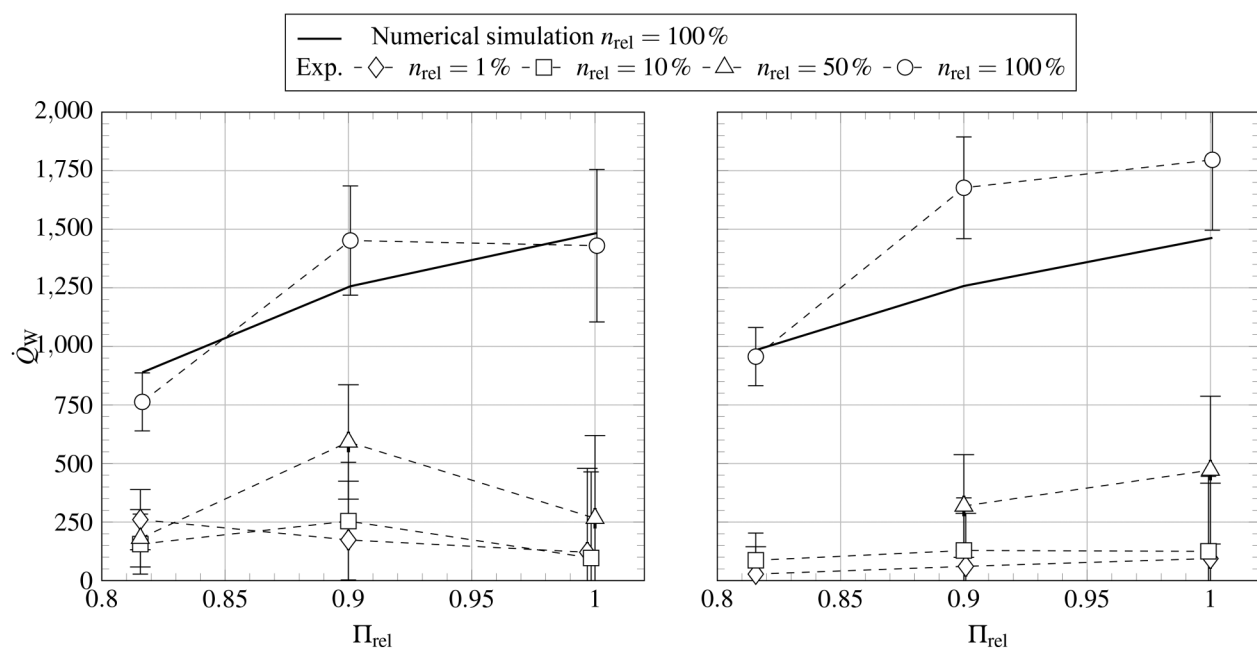

Figure 10. Windage heating for smooth (left) and honeycomb (right) configurations. Error bars indicate 95% confidence interval.
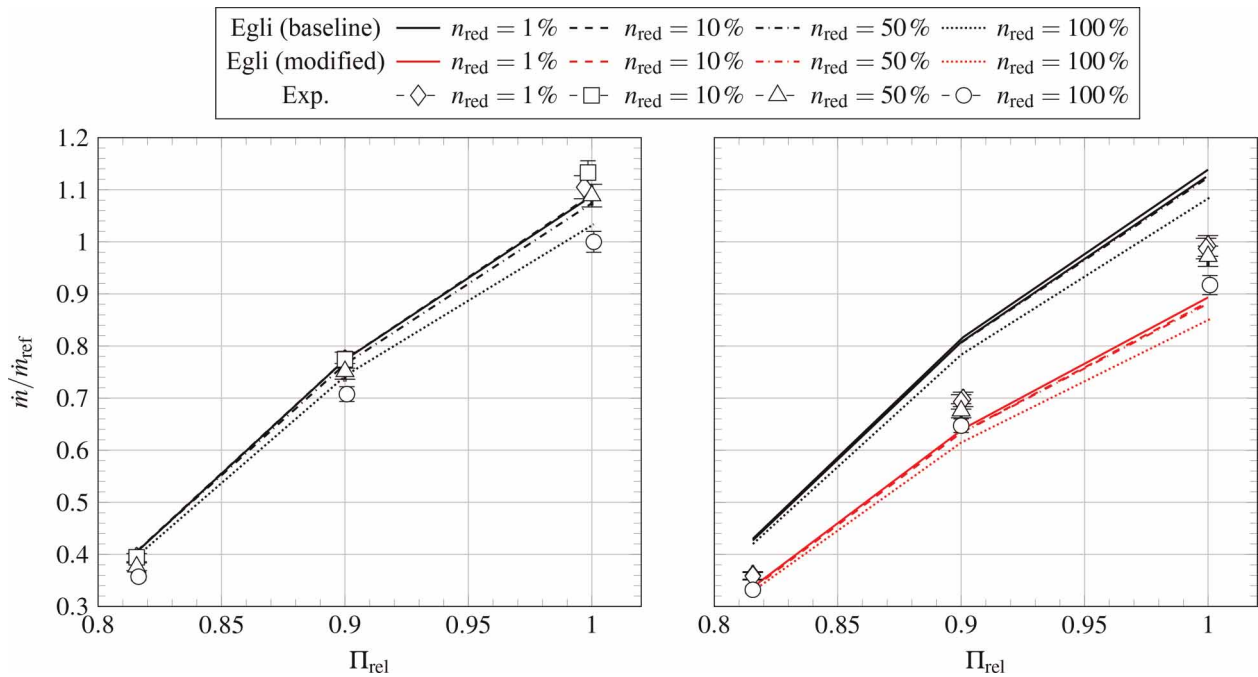
Figure 11. Mass flow rate for smooth (left) and honeycomb (right) configurations. Error bars indicate 95% confidence interval.

Finally, we consider the ability of empirical correlations to predict the mass flow rate of the labyrinth seal. Figure 11 depicts the mass flow rate relative to that at the nominal operating point for the smooth-casing configuration, i.e., $\dot{m}_{\text{ref}} = \dot{m}_{\text{ADP,smooth}}$. Included is the mass flow rate as predicted by the correlation by Egli (1935) using the parameters introduced in the methodology section of this paper. For the smooth configuration, the predicted mass flow rate agrees well for the entire map, albeit the sensitivity to the change in rotational speed appears lower than in the experiment. The deviation to the experimental data equals 3.4% for maximum speed and pressure ratio. For the honeycomb configuration, mass flow is consistently over-predicted across the entire map as a result of not accounting for the change in the effective gap size and increased losses in the swirl chamber when using the original formulation of Egli's correlation. Using the numerical results presented in this paper, we can derive a simple a-posteriori correction for the correlation. Based on the case of $n_{\text{rel}} = 1\%$, the effective area changes compared to the smooth configuration can be obtained by evaluating Fig. 8. Since the gap area A_{gap} remains constant, the flow coefficient becomes a function of jet area only. We observe As the jet wides up to a higher degree for the honeycomb configurations, we obtain a factor of $\xi = (\alpha_{\text{HC}}/\alpha_{\text{Smooth}}) = 1.35$. With the minimum flow area increasing to a lesser degree than the jet area, the contraction coefficient $C_C = (A_{\text{m}}/A_1)$ decreases, $\psi = (C_{\text{C,HC}}/C_{\text{C,Smooth}}) = 0.63$. Introducing both factors to modify Egli's correlation yields

$$\dot{m}_{\text{Egli,mod}} = \frac{\varphi\psi\gamma\xi\alpha A_{\text{gap}}p_{\text{t,in}}}{\sqrt{RT_{\text{t,in}}}} \tag{13}$$

The results of this modification are included in Figure 11. For low rotational speeds, the modified correlation matches experimental results. For higher speeds, deviations increase as the correction factors were only obtained close to zero speed and prescribed for all operating points. This neglects the influence of rotation on dissipation and momentum (widening of the leakage jet) discussed previously. Obtaining correction factors in each operating point could enable a better prediction, but would require pre-existing results and thus defeat the purpose of such a correlation. It can nevertheless be demonstrated, that a correlation is possible when accounting for the effects discussed in this paper.

Conclusions

The aerodynamic performance of labyrinth seals in turbine shroud cavities was experimentally investigated using a rotating rig. Two configurations have been studied, one with a smooth casing and one featuring an engine-typical honeycomb structure.

As an experimental boundary condition, the same operating points, defined by pressure ratio and rotational speed, were investigated for both configurations. Although the effective area increases locally due to the axial positioning of the seal fins relative to the honeycomb, the discharge coefficient decreases for the honeycomb configuration. The main-flow honeycomb interaction region features low-momentum flow with considerable losses. This region is identified as the main difference when it comes to entropy production and resulting flow heating. The split in pressure drop across individual throttlings becomes more evenly distributed for the honeycomb configuration. An investigation into the sensitivity to rotation revealed that the leakage-jet cross-section increases as a function of speed. Higher speeds generally induce higher flow losses regardless of configuration.

Numerical simulations using RANS-based turbulence models are generally able to predict the local flow field in terms of pressure distribution, even capturing the influence of rotational speed on the pressure slope across the swirl chamber. The mass-flow rate is overpredicted by 3.6% for the smooth and 2.6% for the honeycomb configuration. The prediction of flow losses and resulting heating reveals larger deficits in its accuracy which results in estimation errors of integral parameters with a considerably diminished sensitivity.

We observe that correlations originally obtained for inner air seals at the hub reasonably estimate the experimental map despite shroud-typical geometries such as discontinuous steps in the casing contour. The maximum error in mass-flow estimation was found to be 3.4% for the smooth configuration. As the correlation by Egli (1935) does not account for roughness or larger-structure casing treatments, the error increases considerably for the honeycomb configuration, equaling 8.5% in the ADP. Using numerical results, a simple a-posteriori correction is possible by obtaining the changes in area ratios and using them as correction factors. This yields a much better prediction, but the demonstrated sensitivity of the leakage jet to rotation is still not captured.

This paper demonstrated the possibility of correcting for the honeycomb influence. Future research will focus on deriving a correlation that could be applied without detailed knowledge of the flow field. In addition to the steady-state measurements presented in this paper, unsteady measurements above the honeycomb and downstream of the swirl chamber were also conducted. These unsteady measurements may provide additional insight into the dissipation at the honeycomb and resulting loss generation when coupled with scale-resolving simulations.

Nomenclature

Latin symbols

A area
C_C contraction coefficient
C_D discharge coefficient
c_p isobaric heat capacity
C_p pressure coefficient
e relative error
F_S factor of safety
k heat conductivity
$\dot{m}$ mass flow rate
n rotational speed
N number of sealings, number of nodes
p pressure
$\dot{Q}$ heat flux
R gas constant
$\aleph$ refinement ratio
s entropy
$\dot{s}$ entropy production
T temperature
U velocity
x Cartesian coordinate
X axial coordinate

Greek symbols

α flow coefficient (Egli)
κ ratio of specific heats
θ circumferential coordinate
μ molecular viscosity
μ_T eddy viscosity
Π total pressure ratio
φ expansion term
γ carry-over correction factor
ρ density
ρ observed order of accuracy

Subscripts

avg   averaged quantity
eff   effective
id   ideal
in   quantity at inlet
out   quantity at outlet
red   reduced quantity
ref   reference value
rel   relative quantity
t   total quantity
W   windage

Abbreviations

ADP   aerodynamic design point
CFL   Courant-Friedrichs-Levy number
GCI   grid convergence index
EERE   estimated extrapolated relative error
K   cavity
MP   measurement plane
OP   operating point
Pr   Prandtl number

Acknowledgments

Funding sources

Competing interests

Marcel Oettinger declares that he has no conflict of interest. Tim Kluge declares that he has no conflict of interest. Joerg Seume declares that he has no conflict of interest.

References

ASME V&V Committee. (2009). Standard for Verification and Validation in Computational Fluid Dynamics and Heat Transfer: The American Society of Mechanical Engineers. Newyork.

Darwish M. S. (1993). A new high-resolution scheme based on the normalized variable formulation. *Numerical Heat Transfer, Part B: Fundamentals*. 24 (3): 353–371. https://doi.org/10.1080/10407799308955898

Denecke J., Dullenkopf K., and Wittig S. (2004). Influence of preswirl and rotation on labyrinth seal leakage, in Proc. of ISROMAC10.

Denecke J., Dullenkopf K., Wittig S., and Bauer H. J. (2005). Experimental investigation of the total temperature increase and swirl development in rotating labyrinth seals. In Proc. of the ASME Turbo Expo, pp. 1161–1171.

Egli A. (1935). The leakage of steam through labyrinth seals. *Transactions of the ASME*. 57: 115–122.

Franke M., Kügeler E., and Nürnberger D. (2005). Das DLR-Verfahren TRACE: Moderne Simulationstechniken für Turbomaschinenströmungen. In DGLR-Jahrbuch. Deutscher Luft- und Raumfahrtkongress.

Henke M., Wein L., Kluge T., Guendogdu Y., Biester M. H., and Seume J. R. (2016). Experimental and numerical verification of the core-flow in a new low-pressure turbine. In Proc. of the ASME Turbo Expo.

Kato M. and Launder B. E. (1993). The modeling of turbulent flow around stationary and vibrating square cylinders. In 9th Symposium on Turbulent Shear Flows, pp. 10.4.1–10.4.6.

Kluge T., Wein L., Schmierer R., and Seume J. R. (2019). Sensitivity analysis, design, instrumentation, and experimental validation of a novel labyrinth seal rig. In Proc. of the ETC 10.

Kluge T., Lettmann I., Oettinger M., Wein L., and Seume J. R. (2020). Unsteady flow phenomena in turbine shroud cavities. In Proc. of the GPPS Chania Conference.

Li J., Kong S., Yan X., Obi S., and Feng Z. (2010). Numerical investigations on leakage performance of the rotating labyrinth honeycomb seal. *Journal of Engineering for Gas Turbines and Power*. 132 (6): 1–11.

Martin H. M. (1919). Steam leakage in dummies of the ljungstrom turbine. *Engineering*. 1: 1–3.

McGreehan W. F. and Ko S. H. (1989). Power dissipation in smooth and honeycomb labyrinth seals. In Proc. of the ASME Turbo Expo.

Moore J. and Moore J. G. (1983). Entropy production rates From viscous flow calculations: Part I — a turbulent boundary layer flow. In Proc. of the ASME Turbo Expo.

Nayak K. C. and Dutta P. (2015). Numerical investigations for leakage and windage heating in straight-through labyrinth seals. *Journal of Engineering for Gas Turbines and Power*. 138 (1): 1–10. https://doi.org/10.1115/1.4031343

Paolillo R., Moore S., Cloud D., and Glahn J. A. (2007). Impact of rotational speed on the discharge characteristic of stepped labyrinth seals. In Proc. of the ASME Turbo Expo, pp. 1291–1298.

Roache P. J. (1994). Perspective: a method for uniform reporting of grid refinement studies. *ASME Journal of Fluids Engineering*. 116 (3): 405–413. https://doi.org/10.1115/1.2910291

Schramm V., Willenborg K., Kim S., and Wittig S. (2002). Influence of a honeycomb facing on the flow through a stepped labyrinth seal. *Journal of Engineering for Gas Turbines and Power*. 124 (1): 140–146. https://doi.org/10.1115/1.1403460

Stocker H. L., Cox D. M., and Holle G. F. (1977). Aerodynamic performance of conventional and advanced design seals with solid-smooth, abradable, and honeycomb lands. NASA Report CR-135307.

Tipton D., Scott T., and Vogel R. (1986). Analytical and experimental development of a design model for labyrinth seals. AFWAL-TR-85-2103, Vol. 3.

van Albada G. D., van Leer B., and Roberts W. W. Jr. (1982). A comparative study of computational methods in cosmic gas dynamics. *Astron Astrophys*. 108: 76–84.

Waschka W., Wittig S., Scherer T., and Kim S. (1991). Leakage loss and heat transfer in high-speed rotating labyrinth seals: an experimental verification on numerical codes. In Proc. of the IGTC, Vol. 2, pp. 239–247.

Waschka W., Wittig S., and Kim S. (1992). Influence of high rotational speeds on the heat transfer and discharge coefficients in labyrinth seals. *Journal of Turbomachinery*. 114 (2): 462–468. https://doi.org/10.1115/1.2929166

Wein L., Kluge T., Seume J. R., Hain R., Fuchs T., et al. (2020). Validation of rans turbulence models for labyrinth seal flows by means of particle image velocimetry. In Proc. of the ASME Turbo Expo.

Wilcox D. C. (1998). Turbulence Modeling for CFD, 2nd edn. La Cañada, USA: DCW Industries.

Yan X., Li J., Song L., and Feng Z. (2009). Investigations on the discharge and total temperature increase characteristics of the labyrinth Seals with honeycomb and smooth lands. *Journal of Turbomachinery*. 131 (4): 1–8.

Yan X., Li J. and Feng Z. (2010). Effects of inlet preswirl and cell diameter and depth on honeycomb seal characteristics. *Journal of Engineering for Gas Turbines and Power*. 132 (12): 1–13.

Zimmermann H. and Wolff K. (1998). Air system correlations Part 1: labyrinth seals. In Proc. of the International Gas Turbine and Aeroengine Congress.